PURPOSE-LED PUBLISHING™

PAPER • **OPEN ACCESS**

Single-layer MoSeN – a synthetic Janus two-dimensional transition-metal compound grown by plasma-assisted molecular beam epitaxy

To cite this article: Xingyu Yue *et al* 2025 *2D Mater.* **12** 025004

View the article online for updates and enhancements.

You may also like

- Ultrabroadband THz probing of anisotropic optical conductivity and plasmonic damping in graphene nanostructures
Jie Ji, Cheng Xiang, Lene Gammelgaard et al.
- Interface engineering of van der Waals heterostructures towards energy-efficient quantum devices operating at high temperatures
Manh-Ha Doan and Peter Bøggild
- Highly sensitive, stretchable, and transparent multidirectional wearable strain sensors based on patterned vertical graphene array
Tianzeng Hong, Haonan Li, Jie Xue et al.

This content was downloaded from IP address 147.8.21.22 on 22/01/2025 at 02:40

2D Materials

OPEN ACCESS

RECEIVED
29 October 2024

REVISED
30 December 2024

ACCEPTED FOR PUBLICATION
6 January 2025

PUBLISHED
15 January 2025

Original content from this work may be used under the terms of the Creative Commons Attribution 4.0 licence.

Any further distribution of this work must maintain attribution to the author(s) and the title of the work, journal citation and DOI.

PAPER

Single-layer MoSeN – a synthetic Janus two-dimensional transition-metal compound grown by plasma-assisted molecular beam epitaxy

Xingyu Yue[1], Yipu Xia[1], Degong Ding[2,3], Weng Fu IO[4], Daliang He[2,3], Chao He[5], Yueyang Wang[1], Hongxia Xue[1], Yuanjun Jin[6], Mengfei Yuan[1], Junqiu Zhang[1], Wingkin Ho[1], Hu Xu[5], Dong-Keun Ki[1], Jianhua Hao[4], Chuanhong Jin[2,3] and Maohai Xie[1,*]

[1] Department of Physics and HK Institute of Quantum Science & Technology, The University of Hong Kong, Pokfulam, Hong Kong Special Administrative Region of China, People's Republic of China
[2] State Key Laboratory of Silicon and Advanced Semiconductor Materials, School of Materials Science and Engineering, Zhejiang University, Hangzhou, Zhejiang 310027, People's Republic of China
[3] Jihua Laboratory, Foshan, Guangdong 528200, People's Republic of China
[4] Department of Applied Physics, The Hong Kong Polytechnic University, Hung Hom, Hong Kong Special Administrative Region of China, People's Republic of China
[5] Department of Physics, Southern University of Science and Technology, Shenzhen, Guangdong 518055, People's Republic of China
[6] Guangdong Basic Research Center of Excellence for Structure and Fundamental Interactions of Matter, Guangdong Provincial Key Laboratory of Quantum Engineering and Quantum Materials, School of Physics, South China Normal University, Guangzhou 510006, People's Republic of China
[*] Author to whom any correspondence should be addressed.

E-mail: mhxie@hku.hk

Keywords: single-layer, MoSeN, synthetic, Janus, two-dimensional transition, compounds

Supplementary material for this article is available online

Abstract

Two-dimensional (2D) nanomaterials hold immense application potentials such as in high-performance nano-electronics, and asymmetric 2D structures with inherent electric dipoles will extend the application promises. Yet synthesizing asymmetric 2D structures remains challenging. Herein, we report the first synthesis of single-layer (SL) hexagonal (*H*-) phase polar Janus MoSeN via nitrogen-plasma-assisted molecular beam epitaxy. This is a significant achievement given the incommensurate valence between Mo, Se, and N, and the inherent strain from the Janus architecture. Using an array of compositional and structural characterization methods, we establish the atomic configurations of the synthesized MoSeN SL, confirming that they are 2D Janus transition-metal chalcogen-nitrides rather than alloys. By employing density functional theory calculations and transport measurements, we explore the structural feasibility and offer insights into its electronic properties, demonstrating its metallic behavior with ohmic contact characteristics. Piezoresponse force microscopy measurements reveal vertical piezoelectricity and ferroelectric potentials from the Janus MoSeN SL. Therefore, it exhibits great potential for applications in, e.g. piezoelectric and ferroelectric devices, sensing technologies, and optoelectronic devices. This work not only addresses existing challenges in 2D nanomaterial research but also opens new avenues for the development of advanced functional materials.

1. Introduction

Single-layer (SL) Janus transition metal chalcogenides (TMCs) are atomically thin films of type *MXY*, where '*M*' stands for a transition metal such as Mo while '*X*' and '*Y*' represent two different chalcogen elements (S, Se and Te) straddling the metal plane. Janus TMCs hold many distinct properties different from the widely studied conventional transition-metal dichalcogenide (TMD) monolayers, such as MoS_2. For one, the Janus TMCs exhibit broken mirror symmetry along the vertical axis, leading to, for example, out-of-plane piezoelectricity [1], room-temperature ferromagnetism [2, 3], enhanced Rashba effect [4–6],

© 2025 The Author(s). Published by IOP Publishing Ltd

pronounced high order harmonic generation [7, 8], topological superconductivity [9], and skyrmions [3, 10]. As a result, there is a growing interest in synthesizing two-dimensional (2D) Janus TMCs soon after the first report of a synthetic Janus MoSeS monolayer by Lu *et al* [11]. Currently, two strategies have been adopted to approach 2D Janus TMCs [11–22]. In the first 'one-step' strategy, one plane of chalcogen atoms in the TMD SL (e.g. $MoSe_2$ or WSe_2) are directly replaced by another through sulfurization, achieving MoSeS or WSeS [16, 17, 19–21]. The other, 'two-step', approach consists of hydrogen (H) plasma or electron beam treatment of the TMDs followed by a chosen chalcogen element implantation [7, 11–15, 18, 23]. In the latter process, it is believed that the top layer chalcogen atoms in the TMD SL are stripped off by the remote H-plasma or by high-energy electron beam and then either replaced with H-atoms or remain vacant before finally substituted/-filled up by another chalcogen element upon heating under the chosen chemical environment, giving rise ultimately to the Janus *MXY*. The precise nature of the intermediate states in these processes, however, has not been well studied. Yet they can be critically important in the synthesis of Janus TMCs and hold special places for controlling their atomic configurations and/or stoichiometry. Indeed, the intermediate state of MoSH during the Janus TMC synthesis using H-plasma has been reportedly identified [14]. It was further predicted to own a metallic band structure [11, 14, 24, 25] and superconduct with a relatively high critical temperature ($T_c > 25$ K) [24, 25]. On the other hand, these properties remain to be fully characterized experimentally [14]. Besides, achieving a stable intermediate state during plasma-assisted synthesis of the Janus TMC would lead to an intriguing 2D Janus system that extends the currently studied Janus TMCs. Such non-TMC 2D Janus materials would bring in new properties beyond what the Janus TMC can offer. Firstly, the greater disparity in electronegativity between chalcogen elements and non-chalcogen elements makes non-TMC Janus film much highly polarized along the out-of-plane direction, which could lead to much enhanced piezoelectric effect. Secondly, unlike Janus TMCs where the two chalcogen atoms, though different (e.g. S versus Se), are isoelectronic, in a non-TMC Janus 2D film, there is a valance mismatch between the chalcogen atom layer and the non-chalcogen layer. Together with the inherent strain, it effectively results in heavy doping and alters the electronic band structure dramatically. It also brings a change of phonon modes due to light element implantation. All of these can give rise to novel electronic properties. For example, it can transform a semiconducting TMD layer into a metal and induce superconducting phase transitions at relatively higher critical temperatures. In turn, they may hold additional application potentials than the currently studied Janus TMCs. Therefore, exploring Janus *MXY* compounds, where '*Y*' is an element other than a chalcogen, is highly compelling from both scientific and practical perspectives.

In this work, we report the first synthesis of 2D Janus MoSeN in the hexagonal phase and its reversal to 1*H*–$MoSe_2$ in a molecular-beam epitaxy (MBE) setup equipped with a nitrogen (N) plasma unit. By employing low- and reflection high-energy electron diffraction (LEED/RHEED), annular dark field scanning transmission electron microscopy (ADF-STEM), x-ray/ultraviolet photoelectron spectroscopy (XPS/UPS), and Auger electron spectroscopy (AES), we establish the compositional and structural nature of the synthetic Janus MoSeN. The dynamic processes starting from the pristine $MoSe_2$ to the Janus MoSeN by N plasma treatment and subsequently its reversal back to $MoSe_2$ by selenization are followed in real-time by *in situ* RHEED. Piezoresponse force microscopy (PFM) measurements show vertical piezoelectricity from the Janus MoSeN SL, which is expected by the presence of out-of-plane dipole. The results further suggest ferroelectric potentials. The electronic bands and properties of the Janus MoSeN SL are investigated by density functional theory (DFT) calculations, showing that it is a metal as verified by transport measurements. The feasibility of synthesizing Janus MoSeN is also examined by DFT. The enhancement of phonon modes by the light N element and strong Mo–N bonds hint superconductivity of MoSeN at relatively high temperatures (~20 K).

The successful experimental realization of Janus MoSeN paves the way for exploring new physical phenomena and unlocks various application opportunities. Its piezoelectric and metallic characteristics make it highly suitable for applications such as in sensors for wearable flexible electronic devices and displays. By forming the metallic Janus MoSeN locally may improve ohmic contacts between the metal electrode and TMD devices. The anticipated superconductivity may also open an avenue for superconducting devices, such as superconducting quantum interference device and superconducting circuits for quantum computing. Therefore, MoSeN can be a very versatile material for future exploration.

2. Results and discussions

Pristine $MoSe_2$ was firstly grown on Au(111) by MBE at large scale and with low defect densities [26]. The MBE was equipped with a radio-frequency (RF) plasma unit, by which we treated the grown $MoSe_2$ *in situ* for Janus MoSeN formation. Selectively, we further reversed the synthetic MoSeN back to $MoSe_2$ by selenization. Figure 1(a) schematically depicts the synthesis procedure. The RHEED was adopted throughout to monitor the surface progression and figure 1(b) shows a set of representative RHEED patterns taken at different stages of the sample treatment process. The very top pattern (labeled '**I**') is from the

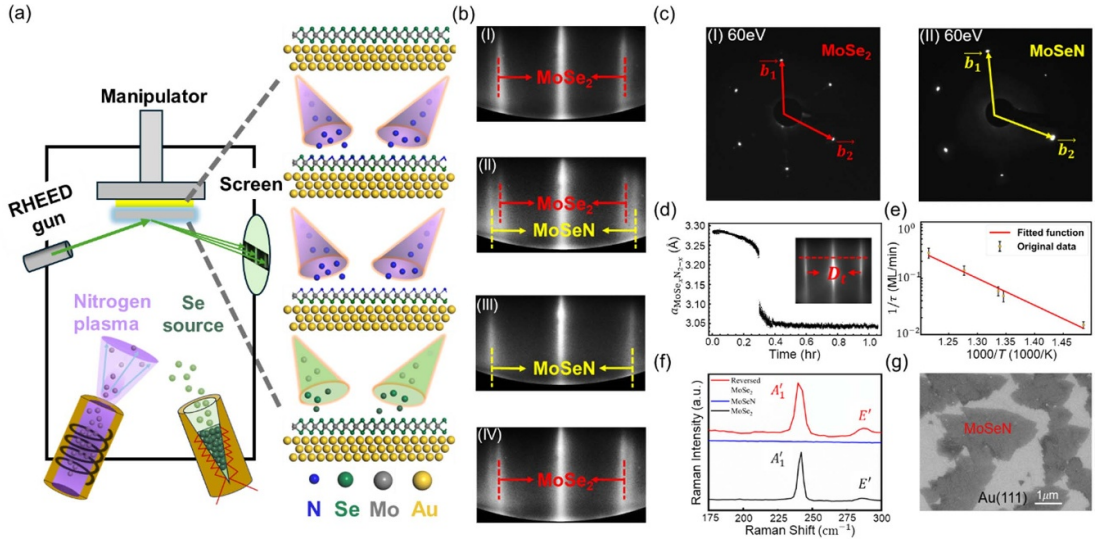

Figure 1. MBE growth of 1*H* Janus MoSeN SL. (a) Schematic illustration of the growth process of MoSeN and its reverse to $MoSe_2$ in a N plasma-assisted MBE setup: initial $MoSe_2$ SL grown on Au(111) substrate is treated by N-plasma, stripping off the top-layer Se and replaced by N atoms, forming the Janus 1*H*-MoSeN SL. The 1*H*-MoSeN SL is reversed back to $MoSe_2$ by selenization. (b) RHEED patterns taken at different stages of the process, from the starting $MoSe_2$ (I), during (II) and after (III) N-plasma treatment, and the recovered $MoSe_2$ by selenization (IV). (c) LEED patterns of (I) $MoSe_2$-on-Au(111) and (II) MoSeN-on-Au(111), taken at 60 eV. (d) Lattice constant evolution during N-plasma treatment as measured by RHEED in real-time. (e) Arrhenius plot and the fitting result of the formation rate of MoSeN at different substrate temperatures, revealing an activated process. (f) Raman spectra of the starting $MoSe_2$ (black), MoSeN (blue), and reversed $MoSe_2$ (red). (g) SEM image of the Janus MoSeN SL on Au(111) substrate.

starting $MoSe_2$ grown on Au(111), where the spacing D between the (01) and $(0\bar{1})$ streaks as marked by the dashed red lines reflects the lattice constant of $MoSe_2$ (i.e. $a_{MoSe_2} \approx 3.33$ Å). When exposed to N-plasma, the surface roughens as reflected by the broadening of the RHEED streaks. A new set of streaks also emerges on the outskirt (see '**II**' in figure 1(b)), indicating a film with a smaller lattice constant than that of $MoSe_2$ starts to form. We tentatively assign the latter to be of $MoSe_xN_{2-x}$. Indeed, the shorter Mo–N bond length than Mo–Se expectedly leads to a compressed lattice. As N-plasma treatment progresses, the diffraction streaks of $MoSe_2$ subsides while the new set of streaks brightens up and also widens until it stabilizes at a value ∼9% more than that of pristine $MoSe_2$ (see '**III**' in figure 1(b) as well as figure 1(d)). We believe latter to correspond to the situation where a full Se layer in $MoSe_2$ has been substituted by N, i.e. the realization of the Janus MoSeN SL. This conclusion will be further confirmed through STEM and other characterization techniques. As $D \propto 1/a$, we may derive the lattice constant, a_{MoSeN}, of MoSeN to be approximately 3.04 Å according to the relation: $a_{MoSeN}/a_{MoSe_2} = D_{MoSe_2}/D_{MoSeN}$, where D_{MoSe_2} and D_{MoSeN} refer to the measured inter-streak spacings of $MoSe_2$ and MoSeN, respectively. For comparison and completeness, after the lattice stabilized at 3.04 Å, we selectively performed the reversal experiments by switching off N-plasma and turning on Se flux again. A gradual change of the RHEED in reverse order, i.e. from that of MoSeN back to $MoSe_2$ was clearly noted ('**IV**' in figure 1(b)), implying the recovery of $MoSe_2$ film. The RHEED results are corroborated by the LEED measurements as exemplified in figure 1(c), which shows two patterns taken from the starting $MoSe_2$ (**I**) and the synthesized MoSeN (**II**) films, respectively. As seen, besides the lattice constant change consistent with the RHEED, the LEED also reveals good crystallinity of the samples. In particular, rotation and twin domains are suppressed as indicated by the 3-fold diffraction spots.

Next, we examined the temperature dependence of MoSeN formation. While similar behavior was observed over a wide range of temperatures, the rate of MoSeN formation clearly varies. We specifically recorded the time τ taken for the MoSeN pattern to stabilize under different substrate temperatures T and plotted in figure 1(e) in an Arrhenius plot, revealing an activated process according to $\frac{1}{\tau} \propto e^{-E/k_B T}$, where k_B is the Boltzmann constant and E is the energy barrier of the process. This behavior suggests that knocking out the Se atoms from $MoSe_2$ and substituting them by N was not caused solely by the kinetic energy of N atoms from plasma, but also by temperature. By a least-square fitting of the data, we derive a value of the activation energy, $E \sim 0.95$ eV.

We have also adopted Raman spectroscopy to identify the bonding characteristics of the synthesized MoSeN but to no avail because, as will be shown later, it is metallic. On the other hand, for semiconducting 1*H*-$MoSe_2$ obtained by reversal from MoSeN, we did observe both the out-of-plane A_1' mode at 240 cm^{-1} and the in-plane E' mode at 285 cm^{-1}, consistent with that from the starting pristine $MoSe_2$ film as

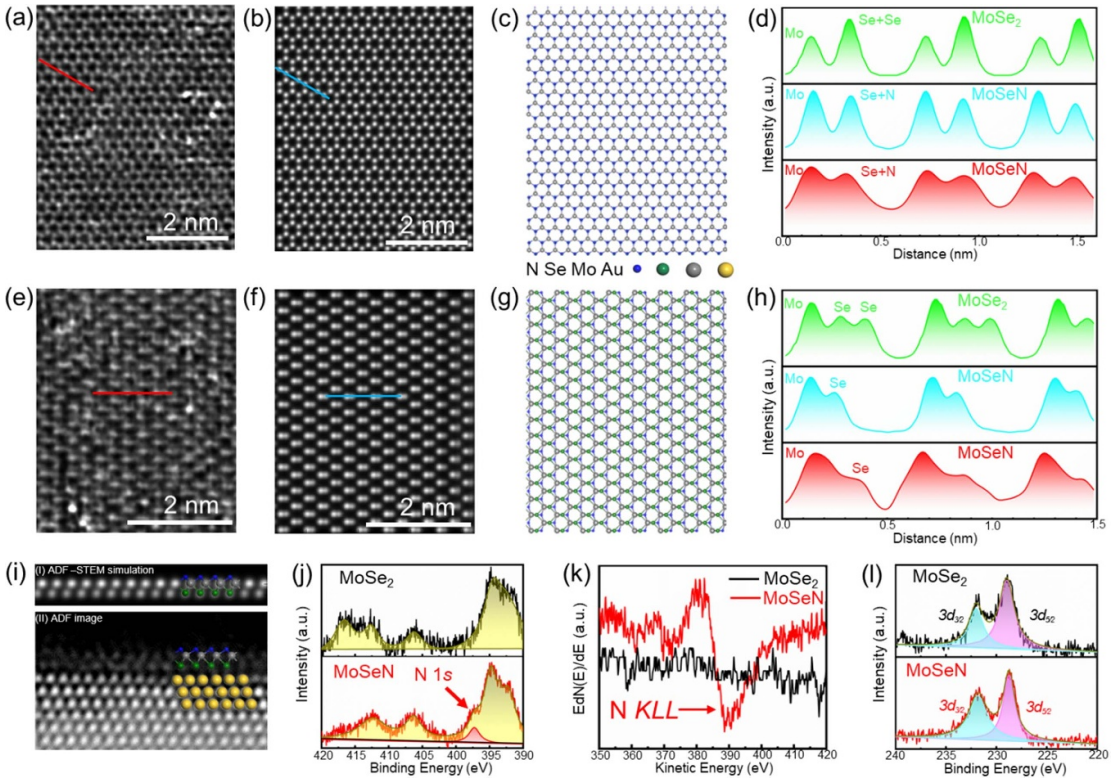

Figure 2. Structural and compositional characterizations of the Janus 1*H* MoSeN SL. (a) On-axis plan-view ADF-STEM image of the synthesized Janus MoSeN. (b) QSTEM simulated plan-view image of the Janus 1*H*-MoSeN SL, where the model is presented in (c). (d) Line profiles (bottom and middle) of the experimental image along the red line drawn in (a) and the simulated one along the cyan line in (b), respectively. For comparison, a line profile taken from a QSTEM simulated image of a pristine $MoSe_2$ SL (not shown) is also presented at the top (green). (e) ADF-STEM of the Janus MoSeN film taken at 20° tilt angle relative to the surface normal. (f) QSTEM simulated image of the Janus 1*H*-MoSeN SL at the 20° tilt angle, where the model is shown in (g). (h) Line profiles (bottom and middle) of the experimental and QSTEM simulated image of Janus 1*H*-MoSeN SL viewed at 20° from surface normal, taken along the red and cyan lines as marked in (e) and (f), respectively. For comparison, the line profile taken from a QSTEM simulated image of a pristine $MoSe_2$ SL (not shown) at 20° is also presented at the top (green). (i) Simulated (top) and experimental (bottom) cross-sectional STEM images of the Janus 1*H*-MoSeN SL, where the experimental one has the Au substrate. (j) XPS of $MoSe_2$ and MoSeN, showing the presence of N in N-plasma treated film. (k) AES of $MoSe_2$ and MoSeN, showing the N *KLL* peak in N-plasma treated film. (l) XPS of $MoSe_2$ and MoSeN, showing the chemical shift of the Mo $3d_{5/2}$ and $3d_{3/2}$ peaks in MoSeN compared to $MoSe_2$.

shown in figure 1(f). The morphology of the synthesized MoSeN was examined by scanning electron microscopy (SEM). Figure 1(g) presents an example where the coverage was purposely made less than a full layer to intentionally reveal the contrast difference between MoSeN and the substrate. Essentially, the sample retained more or less same triangular domains, although damages in microscopic scales were evitable.

To characterize the atomic configurations of N-plasma treated samples, we resorted to STEM, both in plan- and cross-sectional views. For the former, we further experimented at two incidence angles: on-axis and at 20° tilt from the surface normal. The results are presented in figures 2(a)–(e), respectively. From figure 2(a), one firstly notes that the N-plasma treated film takes the same hexagonal ring structure as pristine $MoSe_2$, though the contrast within a honeycomb ring appears more uniform than the 3-fold rings of a pristine $MoSe_2$ SL (see supplementary information figure (S1)). Indeed, quantitative STEM simulations (QSTEM) of the 1*H*-phase Janus MoSeN SL (figure 2(b)) reveals similarly uniform rings, while line profile analysis depicted in figure 2(d) from the experimental data (shown in red, taken along the red line in figure 2(a)) also matches well with the simulated profile from a 1*H* Janus MoSeN (shown in cyan, taken along the cyan line in figure 2(b)), but less so with the simulated data from a 1*H* $MoSe_2$ SL (green). More supporting results about the Janus MoSeN comes from ADF-STEM imaged at the 20° tilt angle (figure 2(e)). As seen from figure 2(h), the intensity profile (red) correlates well with that (cyan) of the simulated one of a Janus MoSeN and is in odd with that of a $MoSe_2$ SL (green). Therefore, we assert that a Janus MoSeN film is obtained by N-plasma treatment of $MoSe_2$ SL on Au(111) substrate.

A more convincing result about the Janus MoSeN is obtained by cross-sectional ADF-STEM. Figure 2(i) presents an experimental image (bottom) together with the QSTEM simulation (top) of the Janus 1*H*-MoSeN on Au (111). The light element of N manifests no contrast in ADF-STEM, so it may appear no different from a Se vacancy. But in any case, the

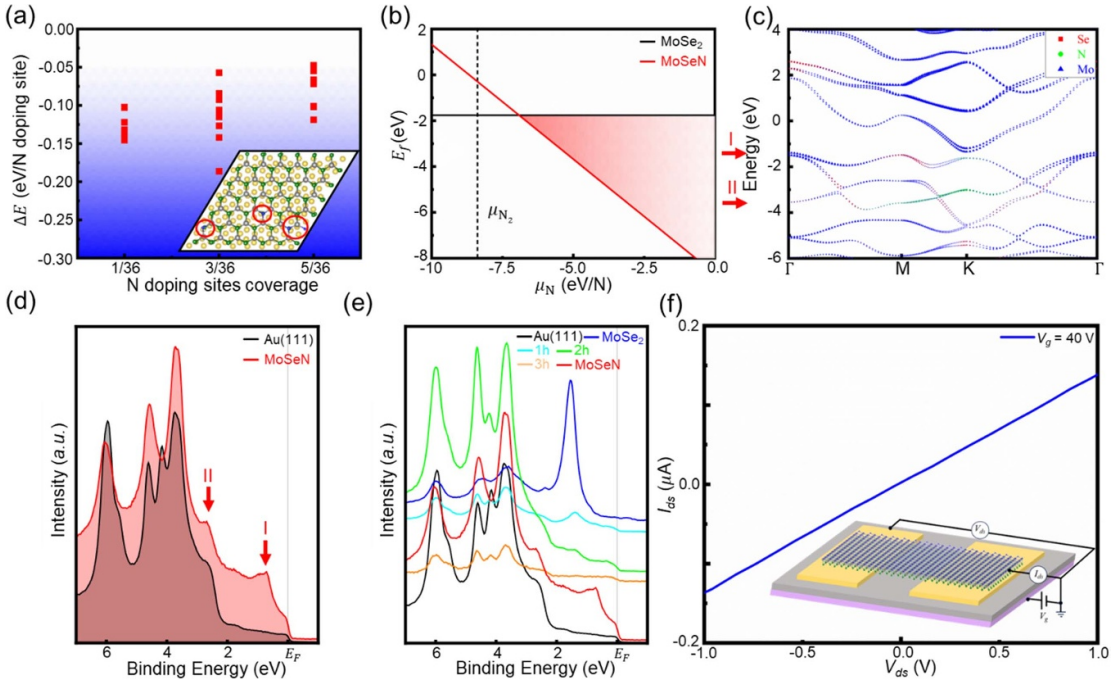

Figure 3. Electronic structure of Janus 1*H*-MoSeN. (a) DFT calculated total energy differences between top- and bottom-layer Se being randomly substituted by N at coverages of 1/36, 3/36 and 5/36 monolayers, respectively. Inset: supercell of 6 × 6 N doped $MoSe_2$ SL on 7 × 7 Au(111) of 3-layer thickness. (b) Formation energies of the Janus MoSeN (solid red line) and pristine $MoSe_2$ SL (solid black line) plotted as a function of nitrogen chemical potential, where $E_f(MoSe_2) = E_{MoSe_2} - E_{Mo} - 2E_{Se}$ for $MoSe_2$ and $E_f(MoSeN) = E_{MoSeN} - -E_{Mo} - -E_{Se} - -\mu(N)$ for the Janus MoSeN. The chemical potential of N_2 is marked by the vertical dashed line for reference. (c) Element-projected band structure of the Janus 1*H*-MoSeN SL. The two red arrows drawn on left mark the two major bands below Fermi level that may have manifested by the two UPS peaks shown in (d), in which spectra of Au(111) (black) and 1*H*-MoSeN SL (red) are shown for comparison. (e) Evolution of UPS spectra obtained at different N plasma dosages, starting from the pristine $MoSe_2$ (blue), at 1 h (cyan), 2 h (green), and 3 h (orange) plasma-treatment at a N_2 flow rate of 1.6 sccm and power of 75 W, finally the Janus MoSeN (red) after 4h treatment. The UPS spectrum of a clean Au(111) is displayed in black. (f) Current–voltage characteristic (I_{ds} versus V_{ds}) of the Janus MoSeN measured at gate voltage $V_g = 40$ V, showing a linear $I_{ds} - V_{ds}$ curve in a wide range of $|V_{ds}| \leqslant 2$ V consistent with the metallic behavior (inset: device schematics). See supplementary information for more details.

Se-layer at the bottom (i.e. adjacent to Au) is seen intact. Therefore nitrogen, if present, must almost all locate on the top plane, consistent with the assignment of a Janus MoSeN SL than an alloy. If it were an alloy, N atoms would have replaced Se randomly in both the top and bottom planes. To show that N does exist, we adopted XPS and AES measurements as presented in figures 2(j) and (k), respectively. In the XPS spectra, the N 1 s peak is discerned in the N-plasma treated sample, whereas no sign of N is identified in the sample before the treatment. In AES, again the treated sample revealed nitrogen KLL transition, while the untreated sample showed no signature of such. In figure 2(l), we show XPS of Mo $3d_{5/2}$ and $3d_{3/2}$ orbitals for both $MoSe_2$ and MoSeN SLs. One notes the chemical shifts of the Mo 3d peaks: from 228.96 eV to 228.74 eV for $3d_{5/2}$ and from 231.99 eV to 231.82 eV for $3d_{3/2}$. These shifts reflect the Mo-N bonding that has caused a change of charge distribution around Mo, affirming again the presence of N that are bonded with Mo in sample.

The Janus MoSeN SL is non-existent in nature. Its formation from $MoSe_2$ upon N-plasma treatment as well as its stability deserve an attention. To this end, we adopted DFT calculations to show firstly that the Janus 1*H*-MoSeN SL adopts the trigonal space group P3m1 (No.156) with a lattice constant of 3.1 Å, which is consistent with our RHEED results of 3.04 Å. Subsequently, we have explored the formation processes of MoSeN from Au-supported $MoSe_2$ SL. Specifically, a 6 × 6 supercell of $MoSe_2$ on 7 × 7 three-layer-thick Au substrate is chosen in the calculation, where the top two layers of Au atoms are allowed to relax while the remaining layer is fixed at the bulk lattice sites. Se in both the top (adjacent to the vacuum) and bottom (adjacent to gold) layers were substituted randomly by one, three, and five N atoms (see figure 3(a)). The energy difference, $\Delta E = E_{top} - E_{bottom}$, between the top- and bottom-layer Se substitution by N were derived. It is found that the ΔE's are consistently less than zero for the three N doping sites coverage (i.e. 1/36, 3/36, and 5/36 monolayers), implying that N substituting Se in the top layer is preferable during the initial N-plasma treatment processes. It aligns with the experimental finding that the Janus MoSeN has the N-layer on top. More importantly, as shown in figure 3(b), the formation energy of the Janus MoSeN can be downshifted to below that of pristine $MoSe_2$ by increasing the chemical potential of N over a critical value. In other

words, at sufficiently high N fluxes, the Janus MoSeN can favorably form. The element-resolved band structure of the Janus 1*H*-MoSeN as calculated by DFT is presented in figure 3(c), revealing a metallic nature of the material. Our UPS measurements as depicted in figure 3(d) reveals two distinct peaks at binding energies of $\sim$ 0.8 eV and 2.7 eV below the Fermi level, which may correlate to the twoΓ-point bands as marked in figure 3(c). To follow the formation process of MoSeN, we progressively treated $MoSe_2$ SL by mild N plasma at different dosages and recorded the UPS spectra: 0, 1-, 2-, 3-, and 4 hours N-plasma treatment at N_2 flow rate of 1.6 sccm and power of 75 W. The formation of MoSeN was seen to be associated with a shift of the binding energy and eventual disappearance of the primary $MoSe_2$ peak below Fermi level E_F but the emergence of new peaks of Janus MoSeN. This aligns with the RHEED results displaying subsiding pattern of $MoSe_2$ and appearance of the new set of diffraction patterns during N-plasma treatment. Transport measurements indicate a linear response over a wide range of drain voltage up to 2 V and ohmic contact behavior of MoSeN film, consistent with the expected metallic characteristics (see figure 3(f) and supplementary information figure S2(b)). Finally, we further obtained the phonon spectra of MoSeN by DFT calculations, which are shown in supplementary information figure S3(a). It is noted that it is devoid of unstable modes in Brillouin zone, substantiating the dynamic stability of the Janus 1*H*-MoSeN SL (see supplementary information figure S3(a)). Besides, the enhanced phonon mode (see supplementary information figure S3(b)) expected from the light N element and strong Mo–N bonds and the added carrier doping per an incommensurate valence between N and Se hint for superconductivity of MoSeN. Furthermore, our study demonstrates that Janus transition-metal chalcogen nitrides based on Nb, Mo, and W are mechanically stable and exhibit superconducting critical temperatures approaching approximately 20 K. For more details, please refer to the supplementary information. Experimental verification of the latter is however hinted by substrate effect and sample quality.

Lastly, mirror symmetry breaking transforms the D_{3h} group $MoSe_2$ SL to the C_{3v} symmetry group of Janus MoSeN SL, which brings in vertical piezoelectricity as predicted in many DFT calculations [2, 3, 27]. In figures 4(a) and (b), we present respectively topographic and piezoelectric amplitude images in the same region of a Janus MoSeN sample on Au(111) measured by resonance-enhanced PFM. In both images, a Janus MoSeN island is highlighted by a dashed red triangle that manifests by different contrasts in the two different measurement modes. Figure 4(c) displays the vertical PFM responses in amplitude and phase; notably, the amplitude signal exhibits clear butterfly-shaped electric hysteresis loops. The phase difference between the two polarization states is 180◦ and the minima in the amplitude loop coincide with the switching voltages in the phase signal, indicating strong piezoelectricity and the possibility of room-temperature ferroelectricity. Our DFT calculations reveal a significant charge imbalance on the two sides of the Mo plane (see figure 4(d)), leading to robust net dipoles along the vertical direction. This elucidates the origin of the experimentally observed piezoelectricity.

We have successfully synthesized single-layer (*H* phase) Janus MoSeN on Au(111) substrates using nitrogen-plasma-assisted MBE. Comprehensive compositional and structural characterizations were conducted using a combination of analytical techniques, including electron diffraction, photoelectron and AES, and ADF-STEM. Nitrogen atoms supplied by the RF-plasma unit substitute selenium atoms in the top plane of $MoSe_2$, leading to the formation of a MoSeN film with broken mirror symmetry. Remarkably, this MoSeN layer can be reversed back to $MoSe_2$ through a simple selenization step. Adopting the RHEED, we have, for the first time, monitored the entire synthesis and reversal processes of MoSeN in real time. Moreover, the temperature dependence of the reaction rate suggests a thermally activated process for plasma assisted MoSeN formation. DFT calculations elucidate the substitution mechanism of nitrogen atoms during the formation and stabilization of MoSeN. Furthermore, DFT results indicate an enhancement of phonon modes, suggesting potential superconductivity. Transport measurements reveal that this synthetic 2D Janus material is metallic, exhibiting ohmic behavior. The broken mirror symmetry in Janus MoSeN leads to out-of-plane piezoelectricity, which has been experimentally verified through PFM. The observations also indicate possible ferroelectricity, offering promise for various device applications. The method we adopted for the synthesis of the Janus MoSeN may be of general applicability, providing a viable route for finely controllable synthesis of other 2D Janus materials with great application potentials in electronics, catalysis, and energy technologies.

3. Methods

3.1. Sample preparation

The growths of $MoSe_2$ thin films were carried out in a customized MBE chamber having a background pressure of $\sim 10^{-10}$ Torr. The flux of molybdenum was generated from an e-beam evaporator operated at the power of $\sim$ 45 W, while that of selenium was provided from a conventional Knudsen cell held at $\sim$ 125 °C. The Se and Mo fluxes were estimated to be $\sim 3 \times 10^{12}$ and $\sim 1.5 \times 10^{11}$ atom/cm^2·s, respectively. Single-crystalline bulk Au(111) substrate was cleaned by successive Argon ion bombardment (1.5 kV, 2×10^{-5} mbar) followed by annealing at $\sim$ 550 °C

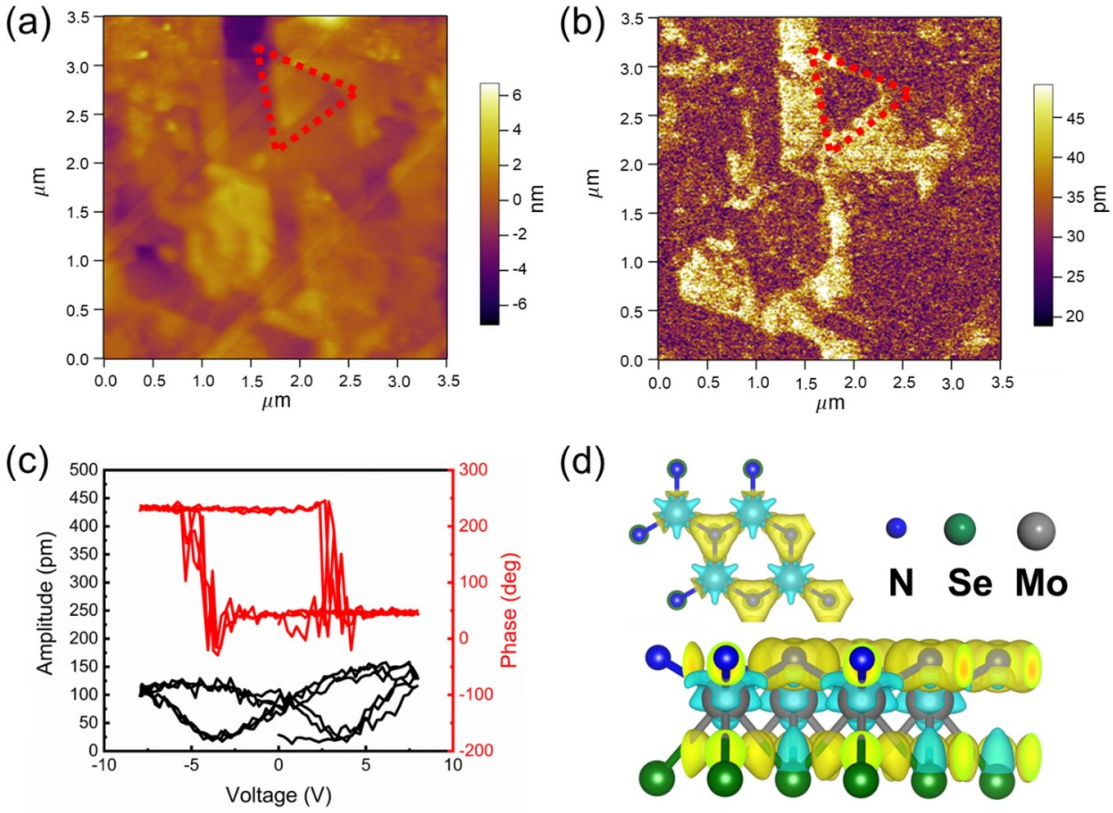

Figure 4. Out-of-plane piezoelectric responses of Janus 1*H*-MoSeN samples. Topographic (a) and piezoelectric amplitude (b) images of the Janus 1*H*-MoSeN SL grown on Au (111), measured by resonance-enhanced PFM. (c) PFM phase (red) and amplitude (black) hysteretic loops taken from the same region of a MoSeN SL. (d) Top- and side-views of charge density difference distribution in Janus 1*H*-MoSeN. Blue, green and gray balls denote N, Se and Mo atoms, respectively. Cyan and yellow colors denote positive and negative charge, respectively.

for at least ten cycles. Nitrogen plasma was generated from RF (13.56 MHz) plasma unit from Oxford Applied Research (HD25). The operation power was 75 W. N_2 flow rate was 1.6 sccm. The substrate temperatures was $\sim$ 400 °C except for the temperature dependent experiments explicitly stated. *In situ* RHEED was conducted using a system from Staib Instrumente, operating at an energy of 10 keV.

3.2. Sample exfoliation

For transport measurement, exfoliation of the grown MoSeN was done by the following procedure: Firstly, polymethylmethacrylate (PMMA) (A4, 950 K) was spin-coated on the Au/mica supported sample at 3000 rpm for 60 s and baked at 120 °C for 90 s. Then hydrofluoric acid was used to etch away mica, which was followed by Au film etching in the gold etchant (potassium iodide).

3.3. STEM characterization and QSTEM simulation

Samples grown on Au bulk crystals or on Au/mica were characterized by ADF-STEM, where the specimen were made by chemical etching and transferred onto a molybdenum-based TEM grid. Atomic-resolution ADF-STEM were performed in a probe-corrected TEM (FEI Titan Chemi STEM G2) operated at 200 kV. The convergence semi-angle was set at 21.4 mrad and the range of acceptance angle of the ADF detector was 53–200 mrad. Cross-sectional STEM specimen was prepared via the focused ion beam (FIB) technique (FEI Helios G4), during which cares like coating of amorphous carbon and platinum as protected layers and low-voltage polishing at 5 kV (48 pA current) were taken to minimize sample damage. As-milled FIB samples were further treated with argon ions (Gatan 691 precision ion polishing system) at 2 kV and 24 pA to remove residual surface contaminations and damage layers. The raw ADF-STEM images were filtered with an improved Wiener filter to improve the signal-to-noise ratio for better display. All the simulated ADF-STEM images were generated by using software QSTEM (ref.Koch, C. T. Determination of Core Structure Periodicity and Point Defect Density Along Dislocations. PhD Thesis, Arizona State University, 2002.), with identical parameter settings to those used in the experimental conditions. Additionally, thermal diffuse scattering was accounted for in all QSTEM simulations.

3.4. PFM measurements

The piezoelectric responses and hysteresis loops measurements were conducted using Scanning Probe Microscope (Asylum MFP-3D Infinity) in dual ac resonance tracking piezo force microscopy mode. A

Pt/Ir coated conductive probe with a force constant of 2.8 N m^{-1} was used in all PFM characterizations under an AC bias V_{ac} of 2–4 V. The Q quality factor was acquired during the contact resonance frequency tuning of the PFM probe and the sample surface.

3.5. DFT calculations

The calculations are performed within the optimized norm conserving Vanderbilt pseudopotentials and general gradient approximation (GGA-PBE) for the exchange-correlation energy functional, as implemented in the QUANTUM ESPRESSO package, with cutoffs of 80 Ry for the wave functions and 320 Ry for the charge density. The Brillouin zone integrations are done with the optimized tetrahedron method on a 40 × 40 Monkhorst-Pack grid k-mesh. The internal atomic positions are fully relaxed with a threshold of 10 meV $Å^{-1}$ for the forces. A vacuum of thickness ∼ 15 Å perpendicular to the monolayer with the inclusion of 2D Coulomb truncation is used to avoid the periodic interactions along the c-axis. The phonon dispersion is calculated within density functional perturbation theory on a 50 × 50 q-mesh using the Phonon module in the QUANTUM ESPRESSO package

3.6. XPS/UPS

Both UPS and XPS measurements were carried out in a separate vacuum chamber connected to the MBE via vacuum interlock. For XPS, Al Kα(1486.6 eV) was adopted, a twin-anode (Mg/Al) x-ray source from VG (Model XR3 × 10^2). For UPS, He I (21.2 eV) was used. The energy analyzer is PHOIBOS100MCD-5 from SPECS.

3.7. AES/LEED

AES measurements were conducted using a digital LEED-AES system (model LOA10-D) at the following settings: a filament current of 1.6 A, Wehnelt voltage of 20.2 V, beam voltage of 1500 V, focus voltage of 1140 V, emission current of 42 μA, and beam current of 38 μA. LEED experiments were performed using a Scienta Omicron SpectalLEED control unit, with a filament current of 1.05 A, screen voltage of 6 kV, and beam voltages ranging from 40 to 200 V.

Data availability statement

The data cannot be made publicly available upon publication because no suitable repository exists for hosting data in this field of study. The data that support the findings of this study are available upon reasonable request from the authors.

Acknowledgment

We are grateful to Xiong Wang and Xiaodong Cui for optical measurements. M. X., D. K., and J. H. acknowledge the financial supports by the Research Grant Council (RGC) of Hong Kong Special Administrative Region (HKSAR), China (Nos. AoE/P-701/20). M. X. also acknowledges the financial support from Guangdong Provincial Quantum Science Strategic Initiative (No. GDZX2301003). D. K. acknowledges the supports by the RGC, HKSAR (Nos. GRF 17300521, 17309722, and 17301424), and J. H. acknowledges the supports from the RGC, HKSAR (Nos. GRF 153025/19P and HKPFS No. PF20-46080). D. D. acknowledges the supports from National Natural Science Foundation of China (Nos. 62404199).

ORCID iDs

Chao He https://orcid.org/0000-0003-3609-5796
Yueyang Wang https://orcid.org/0009-0006-0992-3372
Dong-Keun Ki https://orcid.org/0000-0002-4638-2038
Jianhua Hao https://orcid.org/0000-0002-6186-5169
Chuanhong Jin https://orcid.org/0000-0001-8845-5664
Maohai Xie https://orcid.org/0000-0002-5017-3810

References

[1] Dong L, Lou J and Shenoy V B 2017 Large in-plane and vertical piezoelectricity in Janus transition metal dichalchogenides *ACS Nano* **11** 8242–8
[2] Zhang C, Nie Y, Sanvito S and Du A 2019 First-principles prediction of a room-temperature ferromagnetic Janus VSSe monolayer with piezoelectricity, ferroelasticity, and large valley polarization *Nano Lett.* **19** 1366–70
[3] Liang J, Wang W, Du H, Hallal A, Garcia K, Chshiev M, Fert A and Yang H 2020 Very large Dzyaloshinskii-Moriya interaction in two-dimensional Janus manganese dichalcogenides and its application to realize skyrmion states *Phys. Rev.* B **101** 184401
[4] Hu T, Jia F, Zhao G, Wu J, Stroppa A and Ren W 2018 Intrinsic and anisotropic Rashba spin splitting in Janus transition-metal dichalcogenide monolayers *Phys. Rev.* B **97** 235404
[5] Li F, Wei W, Wang H, Huang B, Dai Y and Jacob T 2019 Intrinsic electric field-induced properties in Janus MoSSe van der Waals structures *J. Phys. Chem. Lett.* **10** 559–65
[6] Li F, Wei W, Zhao P, Huang B and Dai Y 2017 Electronic and optical properties of pristine and vertical and lateral heterostructures of Janus MoSSe and WSSe *J. Phys. Chem. Lett.* **8** 5959–65
[7] Shi J *et al* 2023 Giant room-temperature nonlinearities from a monolayer Janus topological semiconductor *Nat. Commun.* **14** 4953
[8] Petric M M *et al* 2023 Nonlinear dispersion relation and out-of-plane second harmonic generation in MoSSe and WSSe Janus monolayers *Adv. Opt. Mater.* **11** 2300958
[9] Li X-D, Yu Z-D, Chen W-P and Gong C-D 2022 Topological superconductivity in Janus monolayer transition metal dichalcogenides *Chin. Phys.* B **31** 110304
[10] Yuan J, Yang Y, Cai Y, Wu Y, Chen Y, Yan X and Shen L 2020 Intrinsic skyrmions in monolayer Janus magnets *Phys. Rev.* B **101** 094420
[11] Lu A-Y *et al* 2017 Janus monolayers of transition metal dichalcogenides *Nat. Nanotechnol.* **12** 744–9

[12] Zhang K et al 2020 Enhancement of van der Waals interlayer coupling through polar Janus MoSSe J. Am. Chem. Soc. 142 17499–507
[13] Trivedi D B et al 2020 Room-temperature synthesis of 2d Janus crystals and their heterostructures Adv. Mater. 32 2006320
[14] Wan X et al 2021 Synthesis and characterization of metallic Janus mosh monolayer ACS Nano 15 20319–31
[15] Qin Y et al 2022 Reaching the excitonic limit in 2d Janus monolayers by in situ deterministic growth Adv. Mater. 34 2106222
[16] Zhang J et al 2017 Janus monolayer transition-metal dichalcogenides ACS Nano 11 8192–8
[17] Zheng T, Lin Y-C, Rafizadeh N, Geohegan D B, Ni Z, Xiao K and Zhao H 2022 Janus monolayers for ultrafast and directional charge transfer in transition metal dichalcogenide heterostructures ACS Nano 16 4197–205
[18] Han Z, Wei T, Xiao Q, Zhong X, Xiang D and Liu T 2022 Fabrication of patternable Janus transition-metal dichalcogenides assisted by electron beam irradiation Appl. Phys. Lett. 120 221901
[19] Gan Z et al 2022 Chemical vapor deposition of high-optical-quality large-area monolayer Janus transition metal dichalcogenides Adv. Mater. 34 2205226
[20] Jang C W, Lee W J, Kim J K, Park S M, Kim S and Choi S-H 2022 Growth of two-dimensional Janus MoSSe by a single in situ process without initial or follow-up treatments npg Asia Mater. 14 15
[21] Lin Y-C et al 2020 Low energy implantation into transition-metal dichalcogenide monolayers to form Janus structures ACS Nano 14 3896–906
[22] Xue G et al 2023 Modularized batch production of 12-inch transition metal dichalcogenides by local element supply Sci. Bull. 68 1514–21
[23] Guo Y et al 2021 Designing artificial two-dimensional landscapes via atomic-layer substitution Proc. Natl Acad. Sci. 118 e2106124118
[24] Liu P-F, Zheng F, Li J, Si J-G, Wei L, Zhang J and Wang B-T 2022 Two-gap superconductivity in a Janus mosh monolayer Phys. Rev. B 105 245420
[25] Ku R, Yan L, Si J-G, Zhu S, Wang B-T, Wei Y, Pang K, Li W and Zhou L 2023 Ab initio investigation of charge density wave and superconductivity in two-dimensional Janus 2 h/1 t-mosh monolayers Phys. Rev. B 107 064508
[26] Xia Y et al 2023 Wafer-scale single-crystalline MoSe2 and WSe2 monolayers grown by molecular-beam epitaxy at low-temperature—the role of island-substrate interaction and surface steps Nat. Sci. 3 20220059
[27] Yagmurcukardes M and Peeters F 2020 Stable single layer of Janus MoSO: strong out-of-plane piezoelectricity Phys. Rev. B 101 155205